Resonant Optical Antennas
P. Mühlschlegel, *et al.*
Science **308**, 1607 (2005);
DOI: 10.1126/science.1111886

Resonant Optical Antennas

P. Mühlschlegel,[1] H.-J. Eisler,[1] O. J. F. Martin,[2] B. Hecht,[1]* D. W. Pohl[1]

We have fabricated nanometer-scale gold dipole antennas designed to be resonant at optical frequencies. On resonance, strong field enhancement in the antenna feed gap leads to white-light supercontinuum generation. The antenna length at resonance is considerably shorter than one-half the wavelength of the incident light. This is in contradiction to classical antenna theory but in qualitative accordance with computer simulations that take into account the finite metallic conductivity at optical frequencies. Because optical antennas link propagating radiation and confined/enhanced optical fields, they should find applications in optical characterization, manipulation of nanostructures, and optical information processing.

Efficient interconversion of propagating light and localized, enhanced fields is instrumental for advances in optical characterization (*1*–*5*), manipulation (*6*–*8*), and (quantum) optical information processing (*9*–*13*) on the nanometer scale. This requirement recently triggered a search for favorable structures (*1*–*5*, *13*–*21*) and materials (*10*, *22*). Resonant optical antennas excel among other structures by combining (i) field-line concentration at a local shape singularity, that is, a gap (*2*, *3*); (ii) optimum impedance matching to freely propagating waves; and (iii) resonant collective oscillations (plasmons) of the free electron gas (*4*, *5*, *11*, *21*) in the antenna arms. While the field enhancement in the feed gap obviously increases with decreasing width (*20*), variation of the overall antenna length should result in a pronounced resonance in analogy to the radio wavelength regime.

We demonstrate that gold dipole antennas can be designed and fabricated to match optical wavelengths. Upon illumination with picosecond laser pulses, white-light supercontinuum (WLSC) (*23*–*25*) radiation is generated in the antenna feed gap in addition to two-photon photoluminescence (TPPL) (*20*, *26*, *27*) in the antenna arms. The emission from the antennas is more than 10^3 times as strong as that from solid gold stripes of the same dimensions but without feed gap. Variation of the overall length of the antenna reveals a resonance substantially below one-half of the effective excitation wavelength.

The nanometer-scale dimensions of resonant optical antennas raise a twofold experimental challenge, that is, manufacturing with sufficient precision and identification of specific antenna effects. The first challenge can be met by means of modern microfabrication techniques, demonstrated for bow-tie antennas at infrared and, more recently, at optical frequencies (*15*, *16*, *19*, *20*). We fabricated slim dipole antennas with lengths in the half-wavelength range by means of focused-ion beam (FIB) milling. In an initial step, sets of stripes with full length L = 190 to 400 nm and width 45 nm were cut from 40-nm-thick, micrometer-sized rectangular gold patches arranged well separated from each other on an indium tin oxide (ITO)–coated (10-nm thickness) glass cover slide. For complete gold removal, the FIB had to cut slightly into the substrate, leaving a shallow depression (~20 nm) around the stripes. In the final step, one-half of the stripes were converted into optically resonant antennas (ORA) by cutting a narrow groove through the centers of the stripes, leaving an ~20-nm-wide gap between the ORA arms (Fig. 1, A and B). "Resonant" here refers to the laser excitation rather than to WLSC emission, because the permittivity of the substrate and the finite thickness of the antennas reduce the effective wavelength at the interaction zone to values considerably off resonance.

Specific antenna effects were identified with picosecond laser pulses powerful enough to excite WLSC in addition to TPPL and by comparing explicitly the responses of ORAs and stripes. TPPL is a second-order process well documented for gold (*20*, *26*, *27*). WLSC is a fourth-order optical nonlinearity found in various dielectric materials such as glass (*23*, *25*) and water (*24*) but not in gold (*20*, *26*, *27*). WLSC hence provides information on the field enhancement outside the ORA arms. The mechanisms underlying WLSC are not well known but seem to require a minimum pulse length in the picosecond range. Both mechanisms contribute to the "white-light continuum" (WLC) recorded in our experiment, the respective contributions being distinguished by their spectral features and power dependences.

The sample was mounted in an inverted optical microscope modified for confocal operation in reflection (fig. S2A). Laser pulses [center wavelength λ_o = 830 nm, repetition rate 80 MHz, pulse length 8 ps at the sample (figs. S2B and S4), maximum average power 150 μW, which is more than a factor of 5 below damage threshold] were focused (1.3 NA, ∞) to a diffraction-limited spot on the sample. The polarization at the sample was linear and adjustable in direction. The pulses were spectrally cleaned with a line filter before entering the microscope and blocked with a notch filter in front of the detectors. WLC spectra and power dependences of individual structures were obtained at fixed sample positions. WLC emission maps were recorded by scanning the sample with a single-photon-counting avalanche diode (SPAD) detector in combination with an additional bandpass filter (450 to 750 nm) (Fig. 1, C and D). The coincidence of the emission spots with the positions of ORAs and stripes was confirmed with a precision of better than 100 nm by comparison with large-scale scanning electron microscope (SEM) images and optical images (fig. S1). Sizeable WLC emission was found only at the positions of ORAs, for ORAs of a certain length range, and for ORA orientation along the pump polarization (e.g., Figure 1C, antenna #12). The emitted light is polarized along the ORA main axis as well, independent of the excitation polarization, which indicates the importance of the ORA also for the process of WLC emission (fig. S3). For comparison, signals from stripes are barely detectable (Fig. 1C, antenna #16) and are frequently associated

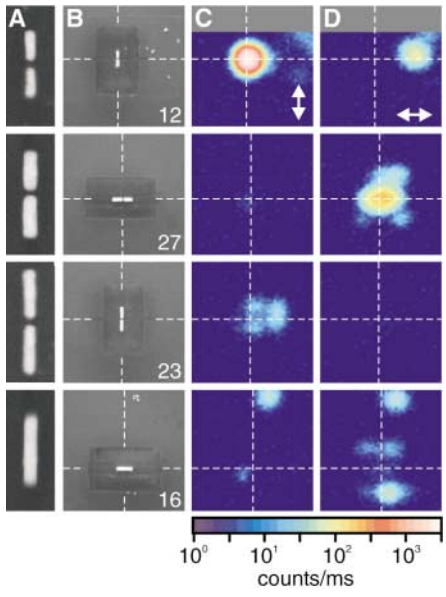

Fig. 1. Examples of ORAs and of a stripe. (**A** and **B**) SEM images, zoom and overview, respectively. (**C** and **D**) Confocal scan images of the WLC generated by vertically and horizontally polarized laser pulses, respectively (average power 110 μW, logarithmic color code). Dimensions: (A) 450 × 180 nm²; [(B), (C), and (D)] 2 × 2 μm². An overview of all ORAs and stripes investigated (including enumeration) is presented in fig. S1.

[1]Nano-Optics group, National Center of Competence in Nanoscale Science, Institute of Physics, University Basel, Klingelbergstrasse 82, CH-4056 Basel, Switzerland. [2]Nanophotonics and Metrology Laboratory, Swiss Federal Institute of Technology Lausanne (EPFL), ELG 240, Station 11, CH-1015 Lausanne, Switzerland.

*To whom correspondence should be addressed. E-mail: bert.hecht@nano-optics.ch

with WLC generation at the rims of the depressions mentioned above.

The WLC spectra (Fig. 2) extend over a considerable range on both sides of the laser line, independent of antenna length. We concentrate here on the short-wavelength wing. At low power, the intensity falls off monotonously toward short wavelengths, typical for TPPL of gold (*26*, *27*). At high power, the spectrum is dominated by a broad peak around 560 nm that we assign to WLSC. Figure 3 shows the dependence of WLC power on laser power for ORAs of different lengths. The log/log curves first rise with slope 2 (dashed lines), which is typical for TPPL. For high-power excitation, the curves follow a fourth-order power law (dashed-dotted lines), supporting the above assignment to WLSC. The nonlinearity of the WLC process was used to determine the laser pulse length right at the position of an ORA by means of the autocorrelation technique (fig. S4). Both Schuck *et al*. (*20*) and Beversluis *et al*. (*27*) report second-order behavior only, although the same materials and a similar range of excitation power are applied. The main differences from the present experiment are the use of femto- instead of picosecond laser pulses and of structures of a different, possibly less favorable, shape.

The variation of WLC power with ORA/stripe length (L) is displayed in Fig. 4A (see also fig. S5) for low- and high-power excitation corresponding to a dominance of TPPL and WLSC, respectively. For the shortest and longest lengths, the antenna emission is about 10 times as strong (30 μW) and 100 times as strong (110 μW), respectively, as the emission of the corresponding stripes. The antenna emission goes through a maximum in between, whereas the stripe emission hardly varies over the whole range of lengths. The ratio of emission intensities reaches values as large as ~30 (antenna #17, L = 258 nm) and ~2000 (antenna #12, L = 250 nm), respectively. The emission data scatter considerably between individual antennas, although Fig. 4A includes only structures that showed a high degree of perfection in the SEM (fig. S1B). This suggests that the WLC emission might be influenced also by material imperfections not visible in the SEM.

We computed the near-field intensity (|electric field|^2) enhancement 10 nm above ORAs and stripes versus length L in steps of 20 nm, using Green's tensor technique (*28*). Figure 4, B to D, reveals drastic differences between antennas and stripes of the same length as well as between antennas of different lengths. This refers to both spatial distribution and amplitude of the enhancement. The strong field concentration in the feed gap of the resonant antenna (Fig. 4C) suggests that WLSC is generated mainly in the underlying ITO/glass substrate, and possibly also in water that might condense inside the gap. Further increase of the enhancement may be expected from reduction of the feed gap width (*20*, *29*).

As a figure of merit for the antenna response, $R(L)$, we use the near-field intensity, integrated, that is, averaged over the whole antenna area plus its immediate environment (600 × 200 nm^2). Although this is a somewhat arbitrary choice, the similarity of $R^2(L)$ and $R^4(L)$ with the experimental data is apparent, showing a flat response for the stripes but a pronounced peak for the ORAs for the same antenna length as in the experiment (Fig. 4A). No fit parameters were used in Fig. 4A except for a scaling factor.

We identify the L_0 ~ 255-nm maximum, seen in experiment and simulation, with the so-called half-wave dipole resonance that might as well be considered a plasmon mode with strong field concentration in the feed gap (Fig. 4B). The latter effect is specific for the optical regime where the permittivity of gold is small (*30*). This prevents the design of ORAs by simple downscaling of radio-wave antennas. WLSC originating from the feed gap volume provides unusual illumination properties that may allow for new forms of local spectroscopy (for instance, single-molecule Raman) and interactions with nanostructures and single-quantum systems.

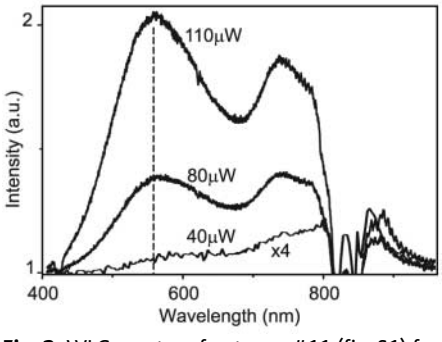

Fig. 2. WLC spectra of antenna #11 (fig. S1) for different excitation powers. Note the increase of the peak at 560 nm for increasing excitation power.

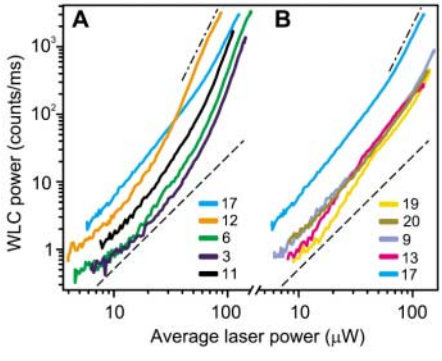

Fig. 3. WLC power dependence of ORAs with different lengths, grouped according to the dominant nonlinearity. (**A**) Fourth order, dashed-dotted line. (**B**) Second order, dashed line.

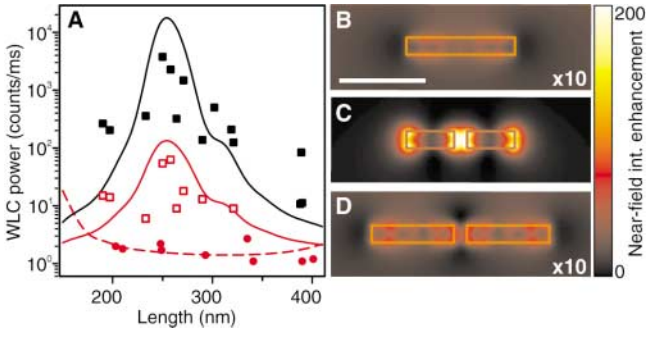

Fig. 4. (**A**) Variation of WLC power with antenna/stripe length. Filled and open squares, ORA at 110 and 30 μW, respectively; circles, stripe at 110 μW (fig. S5); solid red and black curves, $R^2(L)$ and $R^4(L)$ for ORAs, respectively; dashed line, $R^2(L)$ for stripes. (**B** to **D**) Near-field intensity (|electric field|^2) enhancement factor computed 10 nm above a stripe (250 × 40 nm^2), a resonant antenna (250 × 40 nm^2), and an off-resonant antenna (410 × 40 nm^2), feed gap 30 nm, gold on glass, λ = 830 nm, ε = –25.3 + i1.6 (*30*) and 2.25, respectively. Enhancement factor refers to |electric field|^2 of an evanescent field in the absence of the antenna. Scaling factor in (B) and (D), 10x. Scale bar, 200 nm.

References and Notes

1. K. Kneipp *et al.*, *Phys. Rev. Lett.* **78**, 1667 (1997).
2. B. Knoll, F. Keilmann, *Nature* **399**, 134 (1999).
3. A. Hartschuh, E. J. Sanchez, X. S. Xie, L. Novotny, *Phys. Rev. Lett.* **90**, 095503 (2003).
4. J. B. Jackson, S. L. Westcott, L. R. Hirsch, J. L. West, N. J. Halas, *Appl. Phys. Lett.* **82**, 257 (2003).
5. A. J. Haes, W. P. Hall, L. Chang, W. L. Klein, R. P. Van Duyne, *Nano Lett.* **4**, 1029 (2004).
6. L. Novotny, R. X. Bian, X. S. Xie, *Phys. Rev. Lett.* **79**, 645 (1997).
7. H. Xu, M. Käll, *Phys. Rev. Lett.* **89**, 246802 (2002).
8. A. J. Hallock, P. L. Redmond, L. E. Brus, *Proc. Natl. Acad. Sci. U.S.A.* **102**, 1280 (2005).
9. J. R. Krenn *et al.*, *Phys. Rev. Lett.* **82**, 2590 (1999).
10. S. I. Bozhevolnyi, J. Erland, K. Leosson, P. M. W. Skovgaard, *Phys. Rev. Lett.* **86**, 3008 (2001).
11. S. A. Maier *et al.*, *Nat. Mater.* **2**, 229 (2003).
12. W. L. Barnes, A. Dereux, T. W. Ebbesen, *Nature* **424**, 824 (2003).
13. P. Michler *et al.*, *Science* **290**, 2282 (2000).
14. D. W. Pohl, in *Advances in Optical and Electron Microscopy*, T. Mulvey, C. J. R. Sheppard, Eds. (Academic Press, London, vol. 12, 1991), pp. 243–312.
15. R. D. Grober, R. J. Schoellkopf, D. E. Prober, *Appl. Phys. Lett.* **70**, 1354 (1997).
16. Ch. Fumeaux, J. Alda, G. D. Boreman, *Opt. Lett.* **24**, 1629 (1999).
17. D. W. Pohl, in *Near-Field Optics: Principles and Applications*, M. Ohtsu, X. Zhu, Eds. (World Scientific, Singapore, 2000), pp. 22–23 (http://monet.physik.unibas.ch/nfo/members/contact_dp.html).
18. K. B. Crozier, A. Sundaramurthy, G. S. Kino, C. F. Quate, *J. Appl. Phys.* **94**, 4632 (2003).
19. D. P. Fromm, A. Sundaramurthy, P. J. Schuck, G. S. Kino, W. E. Moerner, *Nano Lett.* **4**, 957 (2004).

20. P. J. Schuck, D. P. Fromm, A. Sundaramurthy, G. S. Kino, W. E. Moerner, *Phys. Rev. Lett.* **94**, 017402 (2005).
21. K. Li, M. I. Stockman, D. J. Bergman, *Phys. Rev. Lett.* **91**, 227402 (2003).
22. J. B. Pendry, L. Martin-Moreno, F. J. Garcia-Vidal, *Science* **305**, 847 (2004).
23. R. R. Alfano, S. L. Shapiro, *Phys. Rev. Lett.* **24**, 584 (1970).
24. Y.-D. Qin, D.-L. Wang, S.-F. Wang, Q.-H. Gong, *Chin. Phys. Lett.* **18**, 390 (2001).
25. P.-A. Champert *et al.*, *Opt. Express* **12**, 4366 (2004).
26. G. T. Boyd, Z. H. Yu, Y. R. Shen, *Phys. Rev. B* **33**, 7923 (1986).
27. M. R. Beversluis, A. Bouhelier, L. Novotny, *Phys. Rev. B* **68**, 115433 (2003).
28. M. Paulus, O. J. F. Martin, *J. Opt. Soc. Am. A* **18**, 854 (2001).
29. W. Rechberger *et al.*, *Opt. Commun.* **220**, 137 (2003).
30. P. B. Johnson, R. W. Christy, *Phys. Rev. B* **6**, 4370 (1972).
31. We gratefully acknowledge continuous support by H.-J. Güntherodt. We thank J. Boudaden, I. Mack, and P. Oelhafen for the preparation of ITO substrates, Ch. Schönenberger for providing access to his microfabrication facilities, and Ph. Gasser Eidgenössische Materialprüfungsanstalt (EMPA) for FIB support. We further acknowledge stimulating discussions with J. Y. P. Butter, J. N. Farahani, W. Grange, S. Karotke, A. Lieb, Y. Lill, and J. Toquant. Financial support came from the Swiss National Science Foundation through the National Center of Competence in Research (NCCR) in Nanoscale Science and a research professorship for B.H. O.J.F.M. acknowledges support from NCCR Quantum Photonics.

Supporting Online Material
www.sciencemag.org/cgi/content/full/308/5728/1607/DC1
Figs. S1 to S5

7 March 2005; accepted 20 April 2005
10.1126/science.1111886

Giant Larvacean Houses: Rapid Carbon Transport to the Deep Sea Floor

Bruce H. Robison,* Kim R. Reisenbichler, Rob E. Sherlock

An unresolved issue in ocean science is the discrepancy between the food requirements of the animals living on the deep sea floor and their food supply, as measured by sediment traps. A 10-year time-series study of the water column off Monterey Bay, California, revealed that the discarded mucus feeding structures of giant larvaceans carry a substantial portion of the upper ocean's productivity to the deep seabed. These abundant, rapidly sinking, carbon-rich vectors are not detected by conventional sampling methods and thus have not been included in calculations of vertical nutrient flux or in oceanic carbon budgets.

Most deep benthic communities are supplied with food by a process described more than a century ago as a "rain of detritus" (*1*). The vertical flux of organic carbon in small particles, fecal pellets, and aggregates of marine snow is typically measured by sediment traps (*2*). Most of the particles that reach the deep sea floor are less than 5 mm in size, sink slowly, and have organic carbon levels that are reduced by microbial mineralization during their descent, which may last for months (*3*, *4*). Pulses of small particle flux are coupled to surface productivity (*5*–*7*). In studies of the relationship between organic carbon flux and the nutritional requirements of the deep benthic fauna, there is a discrepancy between the amount of food used by these animals and what can be accounted for by sediment traps on the supply side (*8*–*10*). This gap may be linked to declines in productivity that have accompanied the recent warming of the upper ocean (*9*, *11*–*13*). A number of secondary sources have been suggested that might make up the difference between supply and demand, including carrion falls, pulses of phytodetritus, and lateral transport from continental shelves (*9*, *14*–*16*). All of these probably contribute to the deep benthic food supply, but none have been shown to occur in sufficient quantity or with the consistency necessary to compensate for the disparity.

Here we discuss a class of particles consisting of the large, discarded feeding structures of giant mesopelagic larvaceans (appendicularians). These planktonic tunicates feed on suspended particles by secreting intricate filtration structures made of mucopolysaccharides (Fig. 1A), through which they pump water by beating their tails (*17*). An active filter structure is called a "house" because the animal lives inside it. Typically, each house has two nested filters: a coarse outer mesh and a fine-mesh inner structure. Giant larvaceans attain lengths up to 60 mm, and their houses are frequently greater than a meter in diameter (*17*, *18*).

The first giant larvacean identified, *Bathochordaeus charon*, was discovered in 1898, but their feeding structures were unknown until the 1960s, when they were observed during submersible dives (*18*). Subsequently, giant larvacean houses have been reported by observers using undersea vehicles in the eastern and western Pacific and in the Atlantic (*17*, *19*, *20*). These large houses are very fragile and do not survive capture by plankton nets. As a consequence, their potential contribution to vertical carbon flux was not recognized until they were observed in situ (*21*).

Larvacean houses are disposable, and when one becomes clogged with particles, the animal simply discards it and makes another. The structures collapse when water is no longer pumped through them (Fig. 1B). Once abandoned, they sink rapidly to the sea floor at a rate of ~800 m day^{-1} (*17*). At this rate, there is little time for mineralization by microbes. Discarded houses have not been accounted for by conventional methods for sampling sinking detritus (*22*), and thus their contribution to nutrient flux has not been factored into oceanic carbon budgets (*23*).

We used remotely operated vehicles (ROVs) to measure the abundance of both occupied and discarded giant larvacean houses (called "sinkers") and to collect them for chemical analyses. Abundance was measured by quantitative video transects at 100-m depth intervals, down to 1000 m, on about a monthly basis from 1994 through 2003. By calibrating a camera to record a measured area and then measuring the distance traveled during each transect, we were able to examine a known volume of water at each depth (*24*).

Samples for chemical analysis were collected with specialized samplers by skilled pilots, who carefully positioned the open containers around the delicate sinkers, then gently sealed them inside. Because the sinkers are so very easily fragmented and dispersed, only about 1 in 4 of our collection attempts was successful, and it is easy to see how sediment traps have missed them (*25*). As the sinkers descend, hydrodynamic forces shape them into increasingly compact forms (Fig. 1C); nevertheless, they remain easily disrupted by mechanical contact.

We surveyed the water column at three sites along the axis of the Monterey Canyon, off the California coast. These direct observations revealed a distinct class of large sinking aggregates, clearly derived from giant larvacean houses. The midwater fauna off Monterey Bay contains at least three giant larvacean species, each with a characteristic depth range and a large (>30 cm in diameter), distinctive house (*26*–*28*). The abundance of occupied houses and sinkers varied seasonally and interannually, but both were present year-round (Fig. 2). Estimates of the house-production rate of *Bathochordaeus* range from one per day (*16*) to one per month (*17*). On the basis of our counts of occupied houses, sinkers, and their sinking rate, we calculate that *Bathochordaeus* produces a new house every day (*24*) (Fig. 3). Sinkers are commonly observed during dives along the floor of the Canyon, with densities as

Monterey Bay Aquarium Research Institute, 7700 Sandholdt Road, Moss Landing, CA 95039, USA.

*To whom correspondence should be addressed. E-mail: robr@mbari.org